System identification of a physics-informed ship model for better predictions in wind conditions

Citation for the original published paper (version of record):

Alexandersson, M., Mao, W., Ringsberg, J. et al (2024). System identification of a physics-informed ship model for better predictions in wind conditions. Ocean Engineering, 310(1).
http://dx.doi.org/10.1016/j.oceaneng.2024.118613

Ocean Engineering 310 (2024) 118613

Contents lists available at ScienceDirect

Ocean Engineering

journal homepage: www.elsevier.com/locate/oceaneng

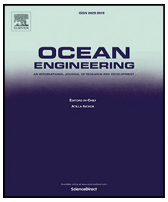

Research paper

System identification of a physics-informed ship model for better predictions in wind conditions

Martin Alexandersson [a,b,*], Wengang Mao [a], Jonas W. Ringsberg [a], Martin Kjellberg [b]

[a] Department of Mechanics and Maritime Sciences, Division of Marine Technology, Chalmers University of Technology, Hörsalsvägen 7A, Gothenburg, 41296, Sweden
[b] Research Institutes of Sweden (RISE), SSPA Maritime Center, Chalmers tvärgata 10, Gothenburg, 41296, Sweden

ARTICLE INFO

Keywords:
Inverse dynamics
KVLCC2
Multicollinearity
Physics-informed manoeuvring model
System identification
Wind-assisted propulsion

ABSTRACT

System identification offers ways to obtain proper models describing a ship's dynamics in real operational conditions but poses significant challenges, such as the multicollinearity and generality of the identified model.

This paper proposes a new physics-informed ship manoeuvring model, where a deterministic semi-empirical rudder model has been added, to guide the identification towards a physically correct hydrodynamic model. This is an essential building block to distinguish the hydrodynamic modelling uncertainties from wind, waves, and currents – in real sea conditions – which is particularly important for ships with wind-assisted propulsion. In the physics-informed manoeuvring modelling framework, a systematical procedure is developed to establish various force/motion components within the manoeuvring system by inverse dynamics regression.

The novel test case wind-powered pure car carrier (wPCC) assesses the physical correctness. First, a reference model, assumed to resemble the physically correct kinetics, is established via parameter identification on virtual captive tests. Then, the model tests are used to build both the physics-informed model and a physics-uninformed mathematical model for comparison.

All models predicted the zigzag tests with satisfactory agreement. Thus, they can indeed be considered as being mathematically correct. However, introducing a semi-empirical rudder model seems to have guided the identification towards a more physically correct calm water hydrodynamic model, having lower multicollinearity and better generalization.

1. Introduction

Ship dynamics predictive models have a wide range of applications, e.g., safety enhancements, and route planning and optimization, autonomous shipping (Aslam et al., 2020). Ship manoeuvring is a sub-field of ship dynamics with well-established system-based models such as Abkowitz (1964), Nomoto et al. (1957), Norrbin (1971), and the MMG (manoeuvring modelling group) model (Yasukawa and Yoshimura, 2015).

The captive model test is the classical method to identify the parameters within these models. However, for full-scale ships, this method is not practical. Computational fluid dynamics (CFD) with either unsteady Reynolds averaged Navier–Stokes (URANS) or steady Reynolds averaged Navier–Stokes (RANS) computations in virtual captive tests (VCTs) has emerged as an interesting option (Liu et al., 2018; Li et al., 2022). CFD requires a complete understanding of the system, which is straightforward for some simplified scenarios, but large modelling uncertainties from wind, wave, and current are expected when applied in a complex sea environment (Miller, 2021). Even if the sea is flawlessly modelled, long-term predictions with high accuracy are exposed to deterministic chaos (Lorenz, 1963). With the other drawbacks of CFD in manoeuvring – such as high computational costs – data-driven models have become an attractive alternative or complement, with an increased number of publications in the past 10–15 years, especially within the field of autonomous ships (Ahmed et al., 2023), where predicting ship trajectories is critical to avoid collisions.

The regressors of the data-driven ship manoeuvring models are often strongly linearly dependent. In the beginning of a turning manoeuvre, side forces are primarily generated by the rudder; But very soon after, the ship will also have a yaw rate and drift angle, so that forces are also generated at the hull surface. The total force acting on the ship is normally used as the dependent variable in the regression, especially when the force from the rudder cannot be measured or estimated. The dependent variable is thus the sum of hull and rudder force,

---

[*] Corresponding author at: Department of Mechanics and Maritime Sciences, Division of Marine Technology, Chalmers University of Technology, Hörsalsvägen 7A, Gothenburg, 41296, Sweden.
E-mail address: maralex@chalmers.se (M. Alexandersson).

https://doi.org/10.1016/j.oceaneng.2024.118613
Received 6 March 2024; Received in revised form 11 June 2024; Accepted 26 June 2024

Nomenclature

α	Rudder angle of attack	C_{D0tune}	Initial drag coeff. tune	T	Thrust
α_f	Rudder inflow angle	C_{D0U}	Initial drag coeff. uncovered	u	Surge vel.
δ	Rudder angle	C_{DC}	Rudder cross-flow drag	v	Sway vel.
δ_{lim}	Rudder gap limit	C_{FC}	Friction coeff. covered	V_∞	Prop. slipstream
$\dot{r}$	Yaw acceleration	C_{FU}	Friction coeff. uncovered	V_A	Apparent vel.
$\dot{u}$	Surge acceleration	C_L	Lift coeff.	V_{RC}	Rudder vel. covered
$\dot{v}$	Sway acceleration	c_r	Rudder root choord	V_{RU}	Rudder vel. uncovered
γ	Prop. induced angle	C_{Th}	Thrust coeff.	V_{RxC}	Axial vel. covered
γ_0	Rudder initial inflow	c_t	Rudder tip choord	V_{RxU}	Axial vel. uncovered
γ_g	Geometric inflow angle	d	lift diminished variable	V_{Ry}	Rudder transverse vel.
$\kappa_{r\gamma g}$	κ_r nonlinear	D_R	Rudder drag	V_{xcorr}	Turbulent mixing
κ_{rtot}	κ_r total	e_0	Oswald efficiency factor	V_{xC}	No turbulent mixing
κ_r	Yaw rate flow straightening	f	lift diminished variable	V_{xU}	No turbulent mixing
$\kappa_{v\gamma g}$	κ_v nonlinear	I_z	Yaw mass intertia	w_f	Taylor wake
κ_{vtot}	κ_v total	K_{gap}		x	Prop. to rudder
κ_v	Drift flow straightening	L_{RC}	Lift covered part	$X_{\dot{u}}$	Surge added mass
λ_R	limited radius of the prop. slipstream	L_{RU}	Lift uncovered part	X_D	Surge damping force
λ	Rudder taper ratio	L_R	Rudder lift	x_G	Center of gravity
ν	Kinematic viscosity	m	Ship mass	X_H	Hull surge force
Ω	Rudder sweep angle	$N_{\dot{r}}$	Yaw added mass	x_H	Yaw rudder interaction
ρ	Water density	$N_{\dot{v}}$	Yaw added mass	X_P	Prop. surge force
a_0	Section lift curve slope	N_D	Yaw damping moment	X_R	Rudder surge force
a_H	Sway rudder interaction	N_H	Hull yawing moment	x_R	Rudder lever
A_{RC}	Rudder area covered	N_P	Prop. yawing moment	X_T	Thrust deduction
A_{RU}	Rudder area uncovered	N_{RHI}	Rudder hull interaction	$Y_{\dot{r}}$	Sway added mass
A_R	Rudder area	N_R	Rudder yawing moment	$Y_{\dot{v}}$	Sway added mass
AR_e	Effective aspect ratio	r	Yaw rate	Y_D	Sway damping force
AR_g	Geometric aspect ratio	r_0	Prop. radius	Y_H	Hull sway force
b_R	Rudder span	r_Δ	Turbulent mixing	Y_P	Propeller sway force
c	Rudder chord	r_∞	Prop. slipstream	y_p	Propeller lever
C_{DC}	Drag coeff. covered	r_x	Prop. slipstream at rudder	Y_{RHI}	Rudder hull interaction
C_{Dtune}	Drag coeff. tunnig	Re_{FC}	Reynold number covered	Y_R	Rudder sway force
C_{DU}	Drag coeff. uncovered	Re_{FU}	Reynold number uncovered	y_R	Rudder lever
C_{D0C}	Initial drag coeff. covered	s	Rudder gap coefficient		

Abbreviations

CFD	Computational fluid dynamics
CMT	Captive model tests
ID	Inverse dynamics
MMG	Manoeuvring modelling group
OLS	Ordinary least-square
PI model	Physics informed model
PU model	Physics uninformed model
RHI	Rudder hull interaction
VCT	Virtual captive tests
WASP	Wind-assisted ship propulsion
wPCC	Wind powered car carrier
SNR	Signal to noise ratio

so that hull and rudder coefficients become strongly linearly dependent in the manoeuvre regression. This multicollinearity is a well-known issue in parameter identification that may lead to parameter drift and poor generalization. The parameters are thus mathematically correct but physically incorrect (Luo, 2016). Using more informative data is perhaps the best way to mitigating the multicollinearity. When that is not feasible, simplifying the model is another commonly researched approach. Other possible remedies are the difference method (Luo, 2016), principal component analysis (PCA), and partial least-squares regression (Jian-Chuan et al., 2015).

Other remedies are however needed. Therefore, a physics-informed manoeuvring model (PI model) is proposed in the present paper, which features a new semi-empirical rudder model to estimate the rudder forces. The rudder and hull forces are then separated in the regression, to reduce the multicollinearity. The PI model is compared to a more conventional physics uninformed model (PU model) with respect to:

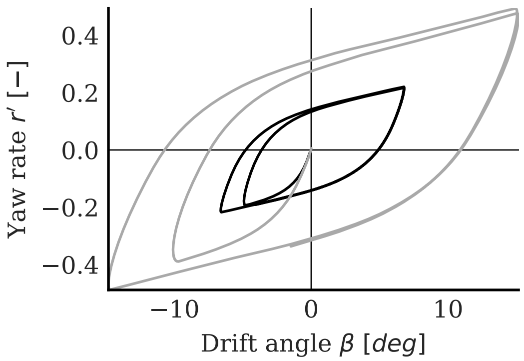

Fig. 1. Phase portrait where the combination of drift angle and yaw rate is shown for zigzag10/10 and zigzag20/20 wPCC model tests.

- Parameter drift.
- Generalization.
- The physical correctness of the identified models.

The parameter drift is studied in a sensitivity analysis. The generalization is studied by exposing a model identified on calm water zigzag tests to wind, which is a state where the ship has a drift angle but no yaw rate. The zigzag test contains little information about this state, as shown in the phase portrait in Fig. 1. There are in fact only six points where the yaw rate is zero, where the phase portrait crosses the x-axis. The physical correctness of the identified PI and PU models is assessed by comparison with a reference model. The reference model is established from virtual captive tests (VCT) based on CFD calculations. This model is assumed to resemble the true hydrodynamics.

A wind-powered pure car carrier (wPCC) is the main test case in the present paper. This ship has much larger rudders than conventional ships – to improve the sailing performance – which increases the demand for physically correct rudder modelling.

A brief description of the workflow of this research is shown in Fig. 2. System identification of the PI and PU models are performed on free sailing model tests (Alexandersson et al., 2022; Alexandersson, 2024) via inverse dynamics (ID) and regression. To assess the physical correctness, a reference model is established, where the PI model is instead identified on a VCT dataset. This reference model, based on CFD, is assumed to be a sufficiently correct representation of the ship's physics. Verification and comparisons between the models are carried out on the free sailing model tests.

The remainder of this paper is organized as follows: The proposed PI model is first presented together with the PU model in Section 2, while mathematical details of the models are given in the appendix. Section 3 describes the developed methodology framework to identify parameters within the PI model, including VCT- and ID-regressions. The case study ship is briefly described in Section 4, along with known parameters of the ship's manoeuvring model. Section 5 provides the results for the wPCC. Results for the KVLCC2 test case are also presented, followed by key conclusions of this research in Section 6.

All code to reproduce this paper is open source (Alexandersson, 2024a).

2. Proposed physics-informed ship manoeuvring model

In this section, the physics informed and uninformed modular manoeuvring models are first introduced. They have identical prediction models for the hull and propeller forces but different models for the rudder forces. The PI model has a new deterministic semi-empirical rudder model, as proposed in this paper (see Section 2.2). The PU model has a data-driven mathematical rudder model. Except for the changed rudder models, the ship manoeuvring models are similar to the MMG model (Yasukawa and Yoshimura, 2015), with some minor enhancements that are presented in the next section.

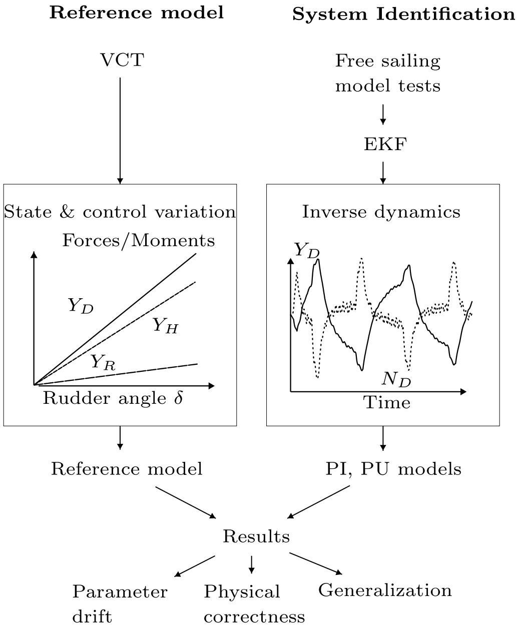

Fig. 2. Research workflow, describing how the reference model is identified with regression of VCT data and the PI and PU models are identified with regression of inverse dynamics forces from model tests. Results are then gathered to assess the parameter drift, physical correctness and generalization of the models.

2.1. Basic manoeuvring model

The ship's kinematics are expressed amidship in a ship fixed reference frame, rotated around the Earth fixed axis x_0 by the heading angle Ψ. Forces and motions are expressed in the surge X, sway Y, and yaw N degrees of freedom as shown in Fig. 3. X_D, Y_D, N_D and u, v, r are the damping forces, moment and velocities in X, Y, N, respectively. The total velocity is defined by the magnitude V and drift angle β. The rudder angle of the two rudders is denoted by δ. The kinematics are described by Eq. (1)–Eq. (3). These equations have the added mass coupling terms, $Y_{\dot{r}}$ and $N_{\dot{v}}$, which are neglected in the MMG model. Subscript D refers to the damping forces and moment (Fossen, 2021), which can be interpreted as the total hydrodynamic force acting on the ship due to the velocity through water.

$$m\left(\dot{u} - r^2 x_G - rv\right) = X_D + X_{\dot{u}}\dot{u} \tag{1}$$

$$m\left(\dot{r} x_G + \dot{v} + ru\right) = Y_D + Y_{\dot{r}}\dot{r} + Y_{\dot{v}}\dot{v} \tag{2}$$

$$I_z \dot{r} + m x_G\left(\dot{v} + ru\right) = N_D + N_{\dot{r}}\dot{r} + N_{\dot{v}}\dot{v} \tag{3}$$

The damping forces and moments are expressed in a modular way, as shown in Eq. (4)–Eq. (6) and Fig. 4,

$$X_D = X_H + X_P + X_R \tag{4}$$

$$Y_D = Y_H + Y_P + Y_R + Y_{RHI} \tag{5}$$

$$N_D = N_H + N_P + N_R + N_{RHI} \tag{6}$$

where subscripts H, P, R, and RHI represent contributions from the hull, propellers, rudders, and rudder hull interaction, respectively. The rudder hull interaction having its own element is a difference from the MMG model.

The hull forces are expressed with the same polynomials as the MMG model, except that the $X_{vvvv}{}'$ coefficient is omitted and an additional resistance term $X_u{}'$ is added to allow for a more nonlinear

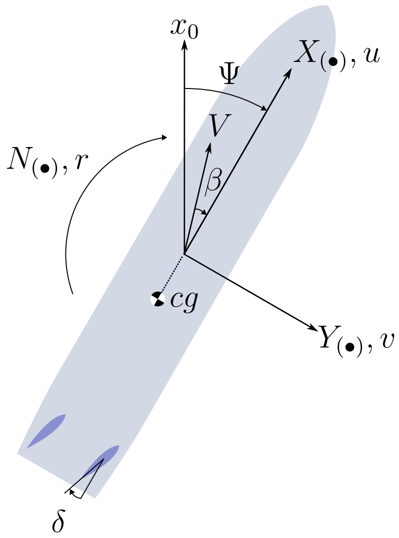

Fig. 3. Relations between the earth fixed and ship fixed reference frames, showing the velocities and forced in the ship fixed frame.

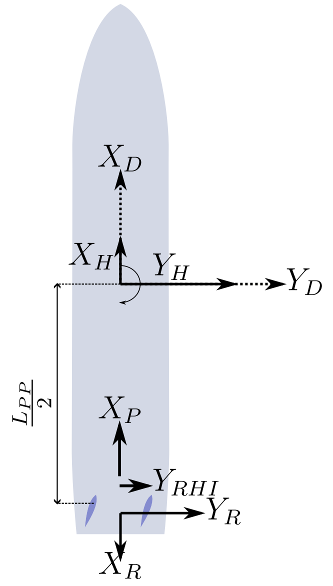

Fig. 4. Modular force components.

resistance (see Appendix A). The nonlinear resistance is possible because of the use of perturbed velocity (see Section 2.3). The total twin screw propeller forces are expressed as

$$X_P = X_{Pport} + X_{Pstbd} \tag{7}$$

$$Y_P = 0 \tag{8}$$

$$N_P = N_{Pport} + N_{Pstbd} \tag{9}$$

The surge forces from the propellers are calculated as the propeller thrust multiplied by a thrust deduction coefficient $X_{Tport} = X_{Tstbd} = (1 - t_{df})$, as in Eq. (10) and a small yawing moment contribution as in Eq. (11), where y_{pport} is the propellers transverse coordinate. The thrusts from the propellers T_{port}, T_{stbd} are taken from the model tests measurements or VCT calculations since modelling of propeller forces is not this paper's focus.

$$X_{Pport} = X_{Tport} T_{port} \tag{10}$$

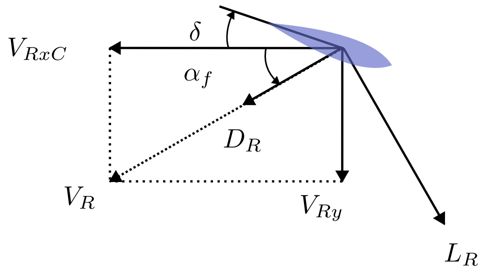

Fig. 5. Inflow to the rudder.

$$N_{Pport} = -X_{Pport} y_{pport} \tag{11}$$

An interaction effect exists between the rudder and hull. The flow in the ship's aft is influenced by the rudder, which generates lift on the hull surface. Forces from rudder actions are thus generated on the rudder and the hull. This effect is modelled by the coefficients a_H and x_H, as shown in Eqs. (12) and (13). This is a changed formulation to the MMG model, avoiding coupled coefficients to simplify for regression.

$$Y_{RHI} = Y_R a_H \tag{12}$$

$$N_{RHI} = N_R x_H \tag{13}$$

The mathematical rudder model (Appendix B.1) is expressed as a truncated third-order Taylor expansion, similar to Abkowitz (1964). The semi-empirical rudder is a new compilation of existing semi-empirical formulas from the literature, presented in the next section.

2.2. *Proposed physical/semi-empirical rudder model*

The semi-empirical rudder model is a lifting line model similar to Kjellberg et al. (2023), Matusiak (2021), and Hughes et al. (2011) that is primarily based on the rudder wind tunnel tests conducted by Whicker and Fehlner (1958). The surge and sway forces are expressed as rudder lift L_R and rudder drag D_R, which are projected on the ship through the rudder inflow angle α_f (see Eq. (14), Eq. (15), and Fig. 5). This angle is the sum of the initial inflow to the rudder at a straight course γ_0 and the inflow to the rudder γ due to propeller-induced speed, drift angle, and yaw rate of the ship, as shown in Eq. (17).

$$X_R = -D_R \cos\left(\alpha_f\right) + L_R \sin\left(\alpha_f\right) \tag{14}$$

$$Y_R = D_R \sin\left(\alpha_f\right) + L_R \cos\left(\alpha_f\right) \tag{15}$$

$$\alpha_f = \gamma_0 + \gamma \tag{16}$$

$$\gamma = \operatorname{atan}\left(\frac{V_{Ry}}{V_{RxC}}\right) \tag{17}$$

The transverse velocity at the rudder V_{Ry} is calculated by multiplying the ship's yaw rate r and transverse velocity v by their flow straightening values κ_{rtot} and κ_{vtot} (Eq. (18)). The flow straightening values have linear and nonlinear dependencies of the geometric inflow angle γ_g (Eq. (21)), as calculated in Eq. (19) with $\kappa_r, \kappa_{r\gamma g}$ and Eq. (20) with $\kappa_v, \kappa_{v\gamma g}$, respectively, so that the flow straightening may vary for different inflow angles, which is an enhancement of the MMG model. The axial velocity at the rudder V_{RxC}, including the velocity of the propeller race, is presented in Appendix B.2.2.

$$V_{Ry} = -\kappa_{rtot} r x_R - \kappa_{vtot} v \tag{18}$$

$$\kappa_{rtot} = \kappa_r + \kappa_{r\gamma g} \left|\gamma_g\right| \tag{19}$$

$$\kappa_{vtot} = \kappa_v + \kappa_{v\gamma g} \left|\gamma_g\right| \tag{20}$$

$$\gamma_g = \operatorname{atan}\left(\frac{-r x_R - v}{V_{RxC}}\right) \tag{21}$$

The yawing moment is modelled as the sway force multiplied by the lever arm x_R, as in Eq. (22).

$$N_R = Y_R x_R \tag{22}$$

2.2.1. Rudder lift

With inspiration from the work of Villa et al. (2020), the total rudder lift is calculated as the sum of the lift at the rudder areas that are covered by the propeller L_{RC} and that at the uncovered area L_{RU}, as shown in Eq. (23) and Fig. 6.

$$L_R = L_{RC} + L_{RU} \tag{23}$$

The lift forces are calculated (Eqs. (24) and (25)) with the lift coefficient C_L. These equations are essentially the same except that the lift at the covered part L_{RC} is diminished by the factor λ_R (Eq. (B.22)) because of the limited radius of the propeller slipstream in the lateral direction (Brix, 1993) (See Appendix B for further details).

$$L_{RU} = \frac{A_{RU} C_L V_{RU}^2 \rho}{2} \tag{24}$$

$$L_{RC} = \frac{A_{RC} C_L V_{RC}^2 \lambda_R \rho}{2} \tag{25}$$

The velocities of the uncovered V_{RU} and covered V_{RC} parts of the rudder are calculated according to Appendices B.2.3 and B.2.2. For a nonstalling rudder, the lift coefficient C_L is calculated according to Whicker and Fehlner (1958) with the additional parameter K_{gap} as shown in Eq. (26).

$$C_L = K_{gap}\left(\alpha \frac{\partial C_L}{\partial \alpha} + \frac{C_{DC}\alpha\left|\alpha\right|}{AR_e}\right) \tag{26}$$

$$\alpha = \delta + \gamma_0 + \gamma \tag{27}$$

The effective aspect ratio AR_e accounts for the mirror image effect when the rudder is flush with the hull, and it is typically assumed to be twice the geometric aspect ratio AR_g (Eqs. (28) and (29)) (Hughes et al., 2011). However, The wPCC rudder is not flush with the hull, so a gap is created between the rudder and rudder horn at larger rudder angles, reducing the pressure difference between the high- and low-pressure sides in the upper part of the rudder. Matusiak (2021) proposed that the gap effect can be modelled as a reduced aspect ratio. Instead, this paper opts for a more straightforward approach based on experience. A factor K_{gap} is introduced, calculated according to Eq. (30). The gap effect is only activated above a threshold rudder angle δ_{lim}, and the strength of the gap effect is modelled by a factor s, as in Fig. 7.

$$AR_g = \frac{b_R^2}{A_R} \tag{28}$$

$$AR_e = 2AR_g \tag{29}$$

$$K_{gap} = \begin{cases} 1 & \text{for } \delta_{lim} > |\delta| \\ s\left(-\delta_{lim} + |\delta|\right)^2 + 1 & \text{otherwise} \end{cases} \tag{30}$$

The lift slope of the rudder $\frac{\partial C_L}{\partial \alpha}$ is calculated using Eq. (31), where a_0 is the section lift curve slope (Eq. (32)) and Ω is the sweep angle of the quarter chord line (Lewis, 1989).

$$\frac{\partial C_L}{\partial \alpha} = \frac{AR_e a_0}{\sqrt{\frac{AR_e^2}{\cos^4(\Omega)} + 4\cos(\Omega) + 1.8}} \tag{31}$$

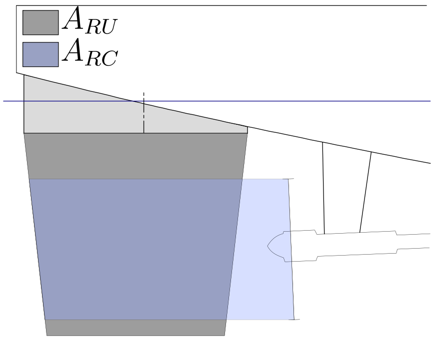

Fig. 6. Rudder areas covered and uncovered by the propeller.

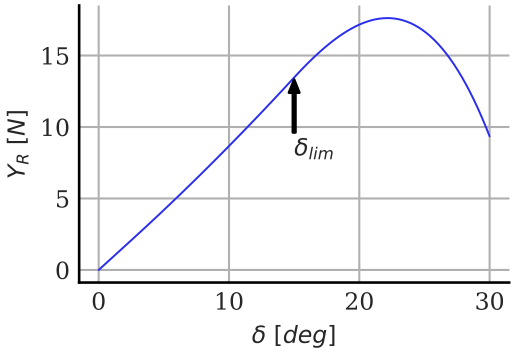

Fig. 7. Rudder lift is reduced by the gap between the rudder and rudder horn for larger rudder angles.

$$a_0 = 1.8\pi \tag{32}$$

Additionally, a small nonlinear part to C_L is modelled by the cross-flow drag coefficient C_{DC}, which is calculated for a rudder with squared tip using Eq. (33), where the taper ratio λ is the ratio between the chords at the tip and the root of the rudder (Eq. (34)) (Hughes et al., 2011).

$$C_{DC} = 1.6\lambda + 0.1 \tag{33}$$

$$\lambda = \frac{c_t}{c_r} \tag{34}$$

2.2.2. Rudder drag

The total rudder drag D_R is calculated as a sum of the contributions from the parts covered and uncovered by the propeller, as in Eq. (35).

$$D_R = 0.5\rho\left(A_{RC} C_{DC} V_{RC}^2 + A_{RU} C_{DU} V_{RU}^2\right) \tag{35}$$

The drag coefficients C_{DC} and C_{DU} are calculated with semi-empirical formulas according to Appendix B.2.1.

2.3. Prime system

Some variables in the equations in this paper are expressed using nondimensional units with the prime system, denoted by the prime symbol (′). Variables are converted from SI units to the prime system using the denominators in Table 1 for the corresponding physical quantity, where U and L are the velocity and length between the perpendiculars of the ship, respectively, and ρ is the water density. For the calculation of surge velocity u', the perturbed velocity $(u - U_0)$ about a nominal speed U_0 is used, as in Eq. (36), to avoid a u' of 1 for all speeds when the ship is on a straight course (where $u = U$), as in a resistance or self-propulsion test. The usage of the perturbed velocity,

Table 1
Scalings with prime system.

Physical quantity	SI unit	Denominator
length	m	L
volume	m^3	L^3
mass	kg	$\frac{L^3\rho}{2}$
density	kg/m^3	$\frac{\rho}{2}$
inertia moment	$kg \cdot m^2$	$\frac{L^5\rho}{2}$
time	s	$\frac{L}{U}$
frequency	1/s	$\frac{U}{L}$
area	m^2	L^2
angle	rad	1
linear velocity	m/s	U
angular velocity	rad/s	$\frac{U}{L}$
linear acceleration	m/s^2	$\frac{U^2}{L}$
angular acceleration	rad/s^2	$\frac{U^2}{L^2}$
force	N	$\frac{L^2U^2\rho}{2}$
moment	Nm	$\frac{L^3U^2\rho}{2}$

Table 2
Parameter variations in virtual captive tests, where a fixed value is indicated by -, ~ means the value varies, and 0 means the variable is zero.

Test type	u	v	r	delta	eta_0
Circle	-	0	~	0	-
Circle + drift	-	~	~	0	-
Circle + rudder angle	-	0	~	~	-
Drift angle	-	~	0	0	-
Rudder and drift angle	-	~	0	~	-
Rudder angle	-	0	0	~	-
Thrust variation	-	0	0	-	~
Self propulsion	~	0	0	0	-

Table 3
Pipeline for the regression from VCT of the PI model.

Test type	Label	Features
Rudder angle	${Y_D}'$	${a_H}'$
Rudder angle	${N_D}'$	${x_H}'$
Self propulsion	${X_H}'$	${X_u}'$ ${X_0}'$
Drift angle	${X_H}'$	${X_{vv}}'$
Drift angle	${Y_H}'$	${Y_v}'$
Drift angle	${N_H}'$	${N_v}'$
Circle	${X_H}'$	${X_{rr}}'$
Circle	${N_H}'$	${N_r}'$
Circle + drift	${X_H}'$	${X_{vr}}'$

therefore, allows for higher order resistance terms in the model, such as X_u, which are otherwise not possible.

$$u' = \frac{u - U_0}{U} \tag{36}$$

For a nondimensional model, U_0 is instead expressed as a Froude number within the model (Eq. (37)), and this paper uses $F_{n0} = 0.02$.

$$F_{n0} = \frac{U_0}{\sqrt{g \cdot L}} \tag{37}$$

3. Proposed method framework to identify PI model

3.1. The reference model

The parameters within the reference model are identified by regression on a VCT dataset, as conducted similarly in Marimon Giovannetti et al. (2020). The VCT involves CFD, where the state was varied according to Table 2. For instance, in the VCT circle test, yaw rate r is varied while surge velocity u is constant, drift angle is zero ($v = 0$), rudder angle is zero, and the propeller is at the self-propulsion point ($\eta_0 = 1$).

The regression is conducted with ordinary least-squares (OLS) multiple linear regression. However, instead of regressing all parameters simultaneously, the regression is divided into many sub-regressions to reduce the multicollinearity. The regressions are defined as a step-wise process in a regression pipeline. The regression pipeline works similarly to solving an equation system. For instance, ${X_{vv}}'$ is determined from the drift angle variation before the circle + drift variation is regressed so that ${X_{vv}}'$ can be used as a known value when ${X_{vr}}'$ is determined. The sub-regressions must thus be performed in the correct order.

The regression pipeline of the reference model is shown in Table 3, where some of the VCT test types (Table 2) are regressed and others are used for validation. Therefore, the semi-empirical rudder is treated as a deterministic model and is not included in the regression. The regression is instead performed on the hull forces X_H, Y_H, N_H obtained from the VCT calculations. However, the total sway force Y_D and total yawing moment N_D are used to determine the rudder hull interaction coefficients ${a_H}', {x_H}'$.

3.2. Inverse dynamics and regression

Inverse dynamics (ID) is a widely used technique within robotics (Faber et al., 2018; Haninger and Tomizuka, 2019-01-12; Mastalli et al., 2023-03-23; Sun and Ding, 2023-11-01; Kurtz et al., 2023-10-11). It can be used to estimate the total forces acting on a ship during motion. The technique can be applied to data from free-model manoeuvring tests or real ship manoeuvres. Estimations of the total damping forces can be solved from the manoeuvring model kinematic equations (Eq. (1)–Eq. (3)). These equations require that the mass, added mass, and full state of the ship are known so that data on the position and orientation of the ship, as well as the higher states, e.g., velocities and accelerations, are known. However, in the model tests used in this paper, only the position and orientation of the ship model were measured. The higher states were thus estimated using an extended Kalman filter (EKF), where the manoeuvring model was used as the predictor (Alexandersson et al., 2022).

The parameter estimations are defined as a linear regression problem (Eq. (38))—one for each degree of freedom.

$$y = \mathbf{X}\zeta + \epsilon \tag{38}$$

The calculations for the label vector y and the feature matrix $\mathbf{X}$ differ for the PU and PI models. The PU model has a data-driven rudder model so that the entire damping forces X_D, Y_D, N_D are included in the regression (Eq. (39)).

$$y = (\bullet)_D \tag{39}$$

where $\bullet$ represents the degrees of freedom (X, Y, N). On the other hand, in the PI model, the deterministic semi-empirical rudder model is excluded from the regression (Eq. (40)).

$$y = (\bullet)_H = (\bullet)_D - (\bullet)_R \tag{40}$$

For example, the regression of the surge degree of freedom label y can be calculated using the ID force (Eq. (41)). The feature matrix $\mathbf{X}$ and coefficient vector ζ are expressed from the model damping force polynomials (Eqs. (42) and (43)), where δ^2 and $X_{\delta\delta}$ are removed for the PI model.

$$X_D = -X_{\dot{u}}\dot{u}' + \dot{u}'m' - m'r'^2 x_{G'} - m'r'v' \tag{41}$$

$$\mathbf{X} = \begin{bmatrix} 1 & u' & (\delta^2) & r'^2 & v'^2 & r'v' \end{bmatrix} \tag{42}$$

$$\zeta = \begin{bmatrix} X_0 & X_u & (X_{\delta\delta}) & X_{rr} & X_{vv} & X_{vr} \end{bmatrix} \tag{43}$$

The hydrodynamic derivatives in the γ vector are estimated with OLS multiple linear regression. In this regression, the hydrodynamic

Fig. 8. Scale model of the wPCC used in the model tests. Copyright RISE.

Table 4
Main particulars (SI units) of the wPCC scale model.

Parameter		Description
B	0.95	Breadth
D	0.12	Propeller diameter
I_{zz}	742.05	Yaw moment of inertia around midship
L	5.01	Length between perpendiculars
T_m	0.21	Mean draught
m	441.03	Ship mass
Scale factor	41.2	
t_{df}	0.12	Thrust deduction factor
x_G	−0.24	Longitudinal c.o.g.

derivatives are treated as Gaussian random variables, and in the manoeuvring model, they are usually estimated as the mean value of each regressed random variable, the most likely value.

Accurate mass and added mass values are more critical when employing ID in a physics-informed model than in a completely data-driven model. The data-driven model can give good simulation results even if the mass and added masses are wrong – if the forces are equally wrong – since the erroneous masses cancel in Newton's second law of motion, as in Eqs. (44) and (45), where ϵ_m is the mass error.

$$F = (m + \epsilon_m) \cdot a \tag{44}$$

$$a = \frac{F}{m + \epsilon_m} = \frac{(m + \epsilon_m) \cdot a}{m + \epsilon_m} \tag{45}$$

When a deterministic force F_R is introduced in the PI model, however, the acceleration contribution a_R of this force is wrong if the mass is wrong (Eq. (46)). Therefore, having correct mass values becomes crucial.

$$a_R = \frac{F_R}{m + \epsilon_m} \tag{46}$$

4. Case study

The wPCC has wind-assisted ship propulsion (WASP) and can alter between a fully sailing mode, and a fully motoring mode, and in between. However, this paper only considers the motoring mode. Because of the WASP, the wPCC design differs slightly from conventional motoring cargo ship designs. The wPCC has two very large rudders, two to three times larger than needed for a conventional ship. The ship also has fins at the bilge to generate extra lift while sailing, as shown on the scale model in Fig. 8. Table 4 shows the main particulars of the scale model.

Required input parameters for the semi-empirical rudder model are summarized in Table 5. The rudder areas where obtained according to Fig. 6. Some manual tuning of the rudder drag was necessary, especially in the neutral rudder case, where the drag was increased almost eight times, as shown by C_{D0tune}. The rudder hull interaction coefficient a_H was set to 0.12, indicating that 12% of the rudder force is generated on the ship hull. Rudder angles greater than 15 degrees (δ_{lim}) were assumed to be affected by the gap between rudder and rudder horn with an estimated strength s based on experience from similar rudder arrangements. The local inflow to the rudders $\gamma_{0port}, \gamma_{0stbd}$ was set to ±2.5 degrees to produce zero lift in the straight-ahead condition. The added mass coefficients are shown in Table 6.

Table 5
Semi-empirical rudder parameters (SI units) in model scale.

Par.		Par.		Par.	
A_{RC}	$1.36 \cdot 10^{-2}$	κ_r	1.17	r_0	$6.07 \cdot 10^{-2}$
A_{RU}	$1.65 \cdot 10^{-2}$	$\kappa_{v\gamma g}$	$3.39 \cdot 10^{-2}$	s	−10
A_R	$3.01 \cdot 10^{-2}$	κ_v	0.89	w_f	0.3
C_{Dtune}	1.08	ν	$1.19 \cdot 10^{-6}$	x	$2.78 \cdot 10^{-2}$
C_{D0tune}	7.82	ρ	1,000	x_H	0.12
Ω	0	a_H	0.13	x_R	−2.45
δ_{lim} $[rad]$	0.26	b_R	0.17	y_{pport}	−0.22
γ_{0port} $[rad]$	$4.4 \cdot 10^{-2}$	c_r	0.15	y_{pstbd}	0.22
γ_{0stbd} $[rad]$	$-4.4 \cdot 10^{-2}$	c_t	0.2		
$\kappa_{r\gamma g}$	1.03	e_0	0.9		

Table 6
Added masses in prime system units.

$X_{\dot{u}}$	$Y_{\dot{v}}$	$Y_{\dot{r}}$	$N_{\dot{v}}$	$N_{\dot{r}}$
$1.79 \cdot 10^{-4}$	$-6.11 \cdot 10^{-3}$	$-3.03 \cdot 10^{-4}$	$-1.28 \cdot 10^{-4}$	$-1.57 \cdot 10^{-4}$

Table 7
Identified hull coefficients in prime system units.

Coefficient	Reference	PI	PU
X'_0	$-1.02 \cdot 10^{-3}$	$-1.02 \cdot 10^{-3}$	$-1.02 \cdot 10^{-3}$
X'_u	$3.35 \cdot 10^{-4}$	$3.35 \cdot 10^{-4}$	$3.35 \cdot 10^{-4}$
X'_{vv}	$-4.83 \cdot 10^{-4}$	$1.69 \cdot 10^{-4}$	$-1.47 \cdot 10^{-2}$
X'_{rr}	$-3.03 \cdot 10^{-4}$	$-1.52 \cdot 10^{-4}$	$-2.3 \cdot 10^{-3}$
X'_{vr}	$2.55 \cdot 10^{-3}$	$3.05 \cdot 10^{-3}$	$-1.01 \cdot 10^{-2}$
Y'_v	$-7.98 \cdot 10^{-3}$	$-9.04 \cdot 10^{-3}$	$-2.07 \cdot 10^{-2}$
N'_v	$-3.21 \cdot 10^{-3}$	$-2.81 \cdot 10^{-3}$	$-1.22 \cdot 10^{-4}$
N'_r	$-1.55 \cdot 10^{-3}$	$-1.58 \cdot 10^{-3}$	$-2.57 \cdot 10^{-3}$

5. Results

The hydrodynamic derivatives within the PI and PU models were identified with inverse dynamics regression (Section 3.2) and the reference model was identified by regression on a VCT dataset (Section 3.1). The identified values are shown in Table 7.

In order to establish the reference model, a comparison with the underlying VCT data is first presented in Section 5.1. The reference model is then used to assess the physical correctness of the identified PI and PU models in Section 5.2. The generalization is then studied on an idealized wind state in Section 5.3. The parameter drift is studied in a sensitivity analysis in Section 5.4. Lastly, results from an additional test case is also briefly studied in Section 5.5 to see how the PI model behaves for a completely different ship type.

5.1. The reference model

The reference model was verified with the underlying VCT data with good agreement as shown in Fig. 9. The ranges of variations were chosen to match the states of the model tests, where, for instance, the drift angle of 10 degrees is the largest recorded from the zigzag tests (Fig. 9(b)). The hull forces are almost linear for these small drift angles and yaw rates. In addition, the higher-order terms in the hull force model (Eq. (A.1)–Eq. (A.3)) were thus omitted in the VCT and ID regressions to reduce the multicollinearity.

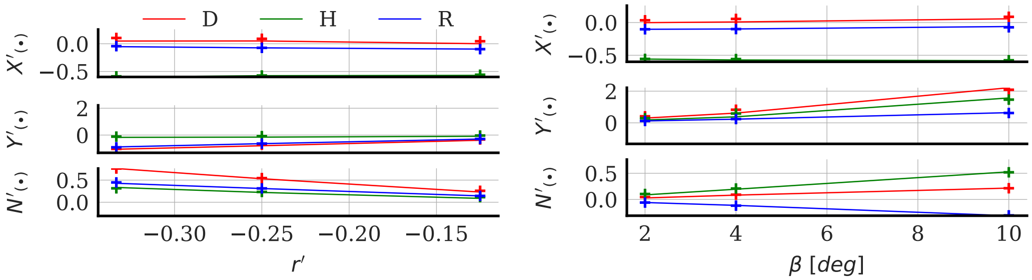

(a) Yaw rates.   (b) Drift angles.

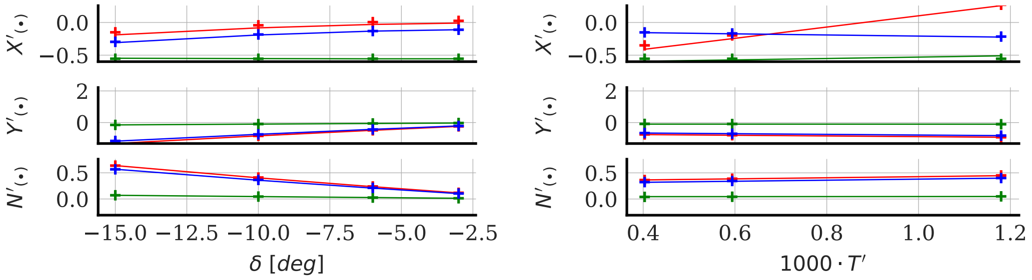

(c) Rudder angles.   (d) Thrust variations at 10 degrees rudder angle.

Fig. 9. Comparison between the VCT data (+) and predictions with the reference model (lines) (expressed in the prime system ×1000) for total damping force D (red), hull force H (green), and rudder forces R (blue).

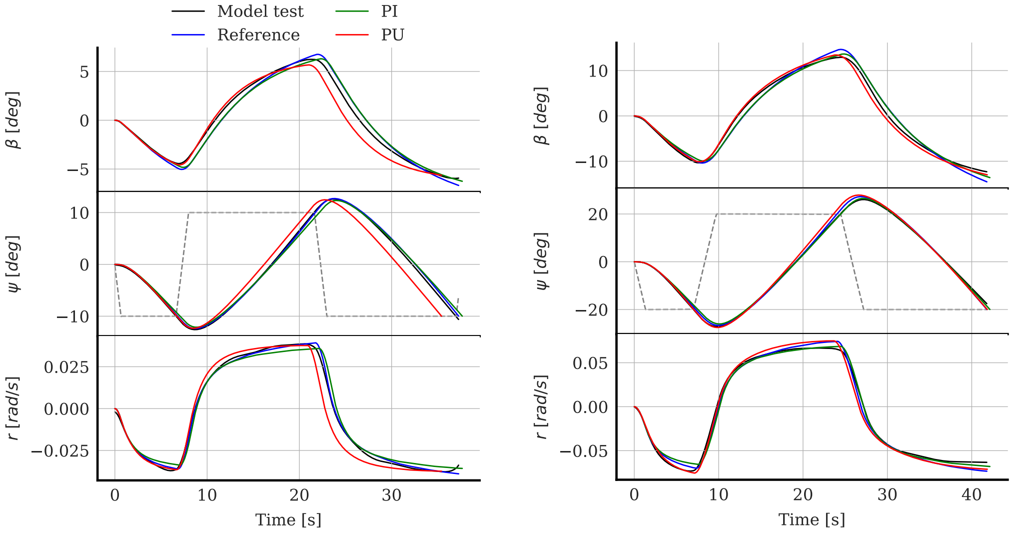

(a) zigzag10/10.   (b) zigzag20/20.

Fig. 10. Closed-loop simulations compared with model test.

5.2. *The physical correctness of the identified models*

The physical correctness of the PI and PU models was assessed by comparisons between the model test experiments and closed-loop simulations as shown in Figs. 10(a) and 10(b). The drift angle β, heading angle ψ, and yaw rate r are in good agreement with the experiments for all the models, especially the heading, which is the most critical in zigzag tests. However, the PU model exhibits a faster response time.

Comparisons of the inverse dynamics forces are shown in Fig. 11 for the zigzag10/10 and in Fig. 12 for the zigzag20/20. This comparison provides more detailed information about the forces and moments involved during the manoeuvres; All models predict the same state in contrast to simulations, where the states may differ as the solutions begin to deviate. The total yawing moments N_D agree well for all models and the experimental data. For the total sway force Y_D, the PU model predicts a slightly higher force.

Furthermore, the reference and PI models predict the same rudder yawing moment N_R since they use the same deterministic semi-empirical rudder model; the yawing moments from the hull N_H are, therefore, also similar for these models. On the other hand, the rudder yawing moment from the PU model is very different. The regression has thus also yielded very different yawing moments from the hull N_H so that the total yawing moment is correct. This can also be seen in the identified $Y_v{}'$, $N_v{}'$, $N_r{}'$ parameter values in Table 7. While the total yawing moment is the same for all models, the decomposition of hull

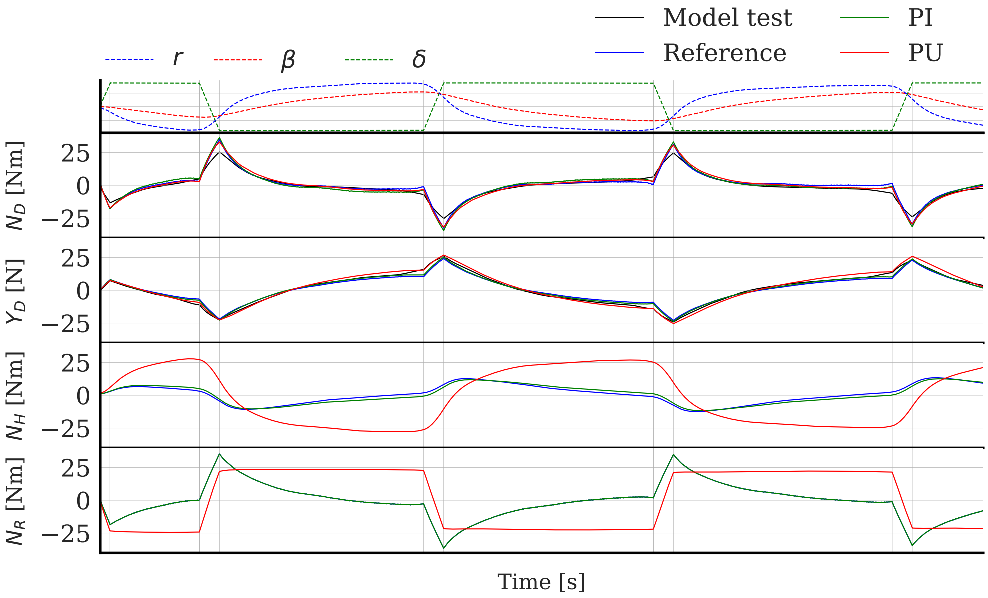

Fig. 11. ID estimations of Y_D and N_D during a zigzag10/10 model test compared with model predictions.

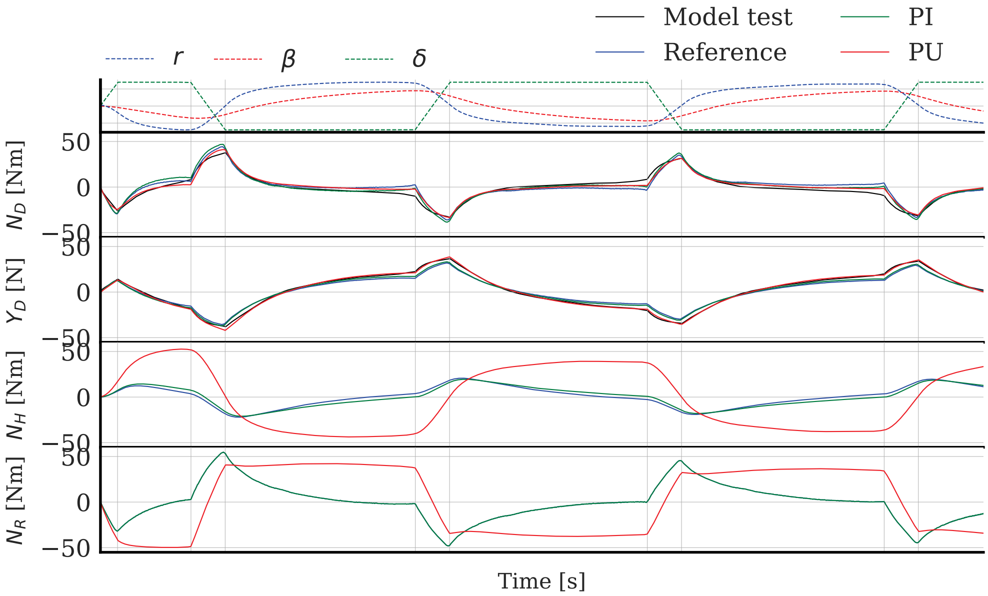

Fig. 12. ID estimations of Y_D and N_D during a zigzag20/20 model test compared with model predictions.

and rudder moments vary significantly. Erroneous decomposition is not a major problem as long as all of the components are active, but if one disappears – e.g., when the rudder angle is small – large errors appear from the remaining components, and the model generalization deteriorates.

The hull force model can be closely examined by decomposing the individual parameter contributions. Fig. 13 shows the parameter decomposition for the two models and the reference model, indicating the contributions for drift and yaw rate parameters so that the drift contribution is given by $N_H(v) = N_v{}'v'$ etc. The PI and reference models have very similar parameter decompositions. However, the parameter decomposition of the PU model is completely different, where almost the entire contribution to the hull yawing moment N_H can be ascribed to the yaw rate parameters. The sway force due to drift is also considerable. How this physically incorrect decomposition affects the model generalization is studied in the next section.

5.3. Model generalization

Predictions were conducted for an idealized wind state to assess the generalization of the identified models. The idealized wind state is a simplified hydrodynamic condition where the models have a drift angle but no yaw rate or rudder angle. This is meant to represent a state in which the ship experiences a static drift angle for an extended period that is induced by a side wind force. Fig. 14 shows the prediction results for the idealized wind condition. The sway force Y_D of the PI model is very similar to that of the reference model. For the PU model, the sway force seems to be too large. The yawing moment N_D is under-predicted by both models, but the difference is more significant for the PU model because most of the yawing moment is attributed to the yaw rate coefficients (as stated in the previous section), which are not activated in the wind state. The PI model seems to have a split between the yaw rate -and drift angle-dependent coefficients in a more similar way to the more physically correct reference model.

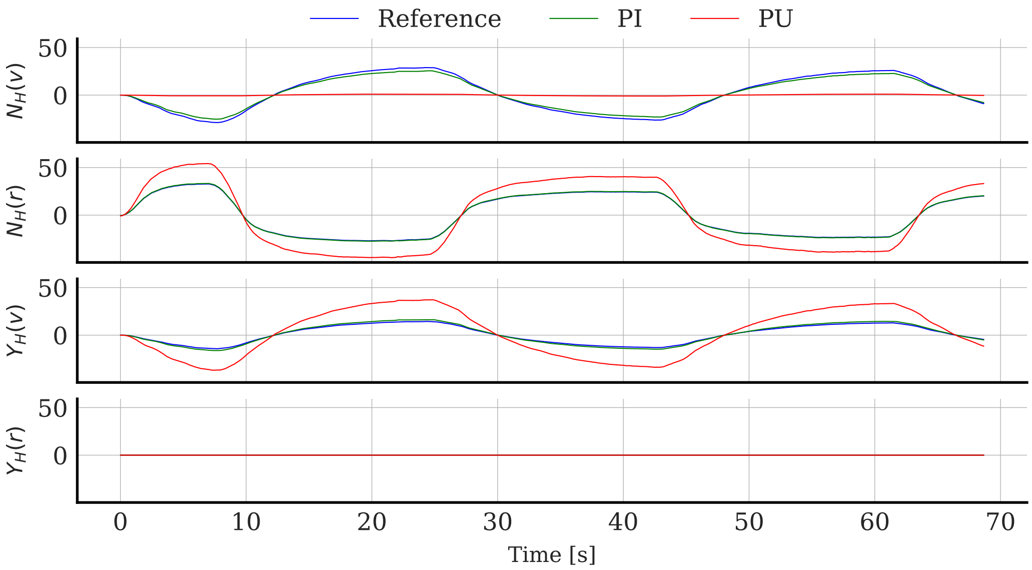

Fig. 13. Decomposition of hull forces and moments during a zigzag20/20 test for parameters related to drift, yaw rate the prediction models.

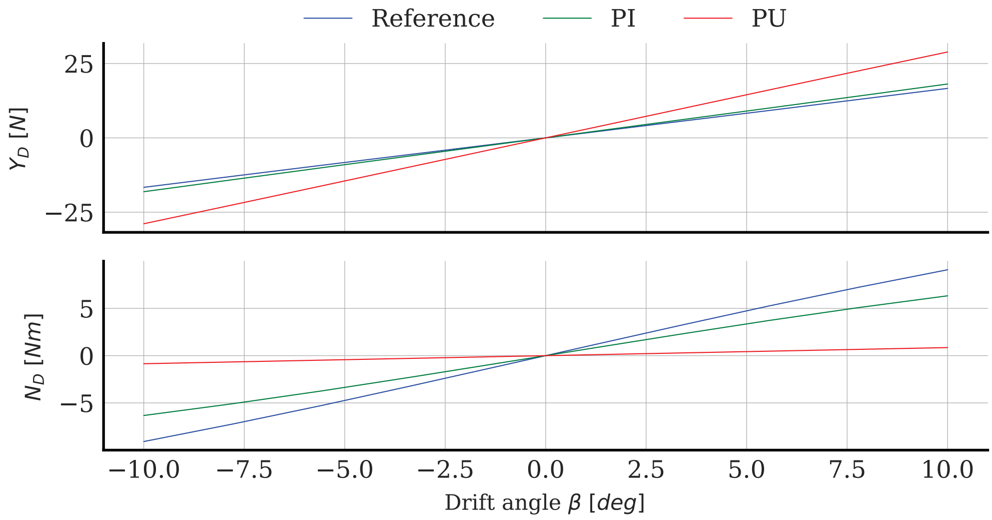

Fig. 14. Total sway force and yawing moment from the wPCC models at various drift angles.

5.4. Parameter drift

The parameter drift of the PU and PI models was studied in a sensitivity analysis, to see how sensitive the models are to small changes in the data. The model test data was filtered with EKF:s with different covariance matrices of the process noise **Q** and observation noise **R**. The observation noise **R** was varied by changing the signal to noise ratio (SNR) according to Eq. (47), where a larger SNR gives a smaller **R**, so that the EKF thereby relies more on the model test data than the predictor model.

$$\mathbf{R} = \frac{\mathbf{Q}}{SNR} \tag{47}$$

Accelerations of the filtered data from one of the zigzag tests with the covariance varied by SNR=0.1, 1, and 10, are shown in Fig. 15. SNR=10 relies more on the data and therefore contains more of the measurement noise. Identified hull coefficients from the data filter variations are shown in Table 8.

Large differences was observed for the PU model, especially in the identified yaw coefficients N'_r, N'_v (also shown in Fig. 16) where N'_v even has the wrong sign for SNR=0.1, and SNR=1.0. The identified values of the PI model is more stable during the variations. The PI model is therefore more robust and less sensitive to small variations in the data.

5.5. Predictions for KVLCC2

A similar but much briefer investigation was conducted for the KVLCC2 test case, to see if similar trends could be observed for the PI and PU models. The models were identified with ID regression on the zigzag10/10 and zigzag20/10 model tests to port and starboard. The model test data were measured from the Hamburg ship model basin (HSVA) for the SIMMAN2008 workshop (Stern et al., 2011). The MMG wake model was added with coefficient values per Yasukawa and Yoshimura (2015). The identified prediction models were compared with captive model tests (CMTs) measured at the Hyundai Maritime Research Institute (HMRI) for the SIMMAN2014 workshop (ITTC, 2017). A comparison for the drift angle variation is shown in Fig. 17. Similar trends to the wPCC in the idealized wind state are evident. The PI model predicts total sway force and yawing moment values that are closer to those of the CMT than those of the PU model, as shown

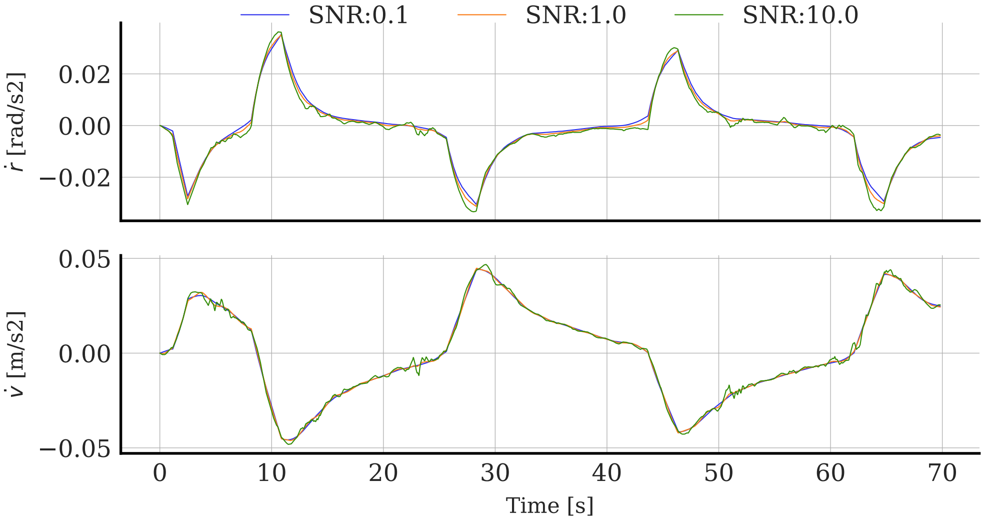

Fig. 15. Kalman filtered yaw and sway accelerations with varying covariance, indicated by the signal to noise ratio (SNR).

Table 8
Identified hull coefficients for the PI and PU models identified on EKF filtered data with varying signal to noise ratio (SNR).

Coefficient	SNR	PI	PU
X'_{vv}	0.1	$2.39 \cdot 10^{-4}$	$-1.45 \cdot 10^{-2}$
	1	$1.01 \cdot 10^{-4}$	$-1.48 \cdot 10^{-2}$
	10	$1.69 \cdot 10^{-4}$	$-1.47 \cdot 10^{-2}$
Y'_{v}	0.1	$-8.83 \cdot 10^{-3}$	$-2.03 \cdot 10^{-2}$
	1	$-8.85 \cdot 10^{-3}$	$-2.03 \cdot 10^{-2}$
	10	$-9.04 \cdot 10^{-3}$	$-2.07 \cdot 10^{-2}$
N'_{v}	0.1	$-2.82 \cdot 10^{-3}$	$3.97 \cdot 10^{-4}$
	1	$-2.83 \cdot 10^{-3}$	$1.8 \cdot 10^{-4}$
	10	$-2.81 \cdot 10^{-3}$	$-1.22 \cdot 10^{-4}$
X'_{rr}	0.1	$-4.97 \cdot 10^{-5}$	$-2 \cdot 10^{-3}$
	1	$-3.05 \cdot 10^{-5}$	$-2.18 \cdot 10^{-3}$
	10	$-1.52 \cdot 10^{-4}$	$-2.3 \cdot 10^{-3}$
N'_{r}	0.1	$-1.57 \cdot 10^{-3}$	$-1.96 \cdot 10^{-3}$
	1	$-1.58 \cdot 10^{-3}$	$-2.21 \cdot 10^{-3}$
	10	$-1.58 \cdot 10^{-3}$	$-2.57 \cdot 10^{-3}$
X'_{vr}	0.1	$3.14 \cdot 10^{-3}$	$-9.65 \cdot 10^{-3}$
	1	$3.13 \cdot 10^{-3}$	$-1 \cdot 10^{-2}$
	10	$3.05 \cdot 10^{-3}$	$-1.01 \cdot 10^{-2}$

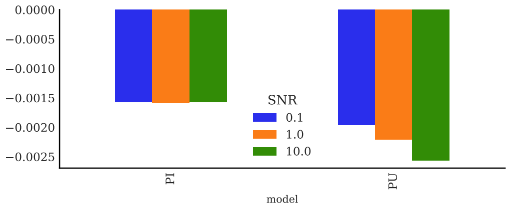

(a) N'_r.

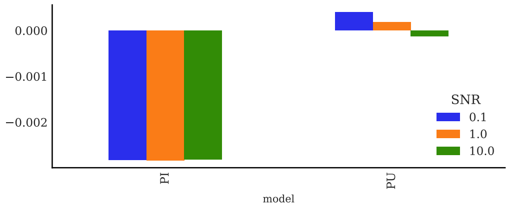

(b) N'_v.

Fig. 16. Identified yaw hull coefficients for the PI and PU models identified on EKF filtered data with varying signal to noise ratio (SNR).

in Fig. 17(a). This can be explained by the PU model's inability to identify the correct rudder forces, as shown in Fig. 17(b). The difference between the reference CMT and the PI model is larger for the KVLCC2 than what was observed in the corresponding comparison for the wPCC (Fig. 14). The KVLCC2 has only one centre rudder compared to the twin rudders of the wPCC and is also a more blunt ship. It is possible that the rudder flow is thus more complicated so that the semi-empirical rudder model presented in this paper is less accurate.

6. Conclusions

This paper investigated whether introducing a semi-empirical rudder model to form a physics-informed manoeuvring model (PI model) would give a more physically correct model — with better generalization. The PI model was identified on two zigzag model tests. The identified model was compared to a similar physics-uninformed model (PU model) and a physically correct reference model to assess: the parameter drift, model generalization and the physical correctness.

All the identified models were found to be mathematically correct since they predicted the model tests with satisfactory agreement. The reference model is the most physically correct model since it predicted both the model tests and VCT accurately. The PU model predicted significantly different forces and moments, thus considered physically incorrect; The regression yielded an incorrect decomposition between the hull and rudder forces and drift angle- and yaw rate-dependent coefficients. Potential problems with the incorrect force decomposition of the PU model were shown in the lack of generalization of an artificial wind state, where the forces and moments had substantial errors. On the other hand, the PI model predicted very similar forces compared to the reference model for the model tests and can, therefore, be considered a more physically correct model. The PI model also has much less parameter drift than the PU model, which was shown in a sensitivity analysis. The models were identified on the model test data with varying levels of filtering, where the PU model was found to be much more sensitive to these small variations.

Introducing a semi-empirical rudder model seems to have guided the identification towards a more physically correct and robust model, with lower multicollinearity and better generalization from calm water zigzag tests to wind conditions.

The PI and PU models were also identified with ID regression on zigzag model tests for the KVLCC2 test case, presenting similar trends. The PI model gave more physically correct predictions than the PU model compared to CMTs, indicating that the conclusions from this paper are not exclusive for WASP ships, such as the wPCC, but also applicable for more conventional ships, such as the KVLCC2. There were

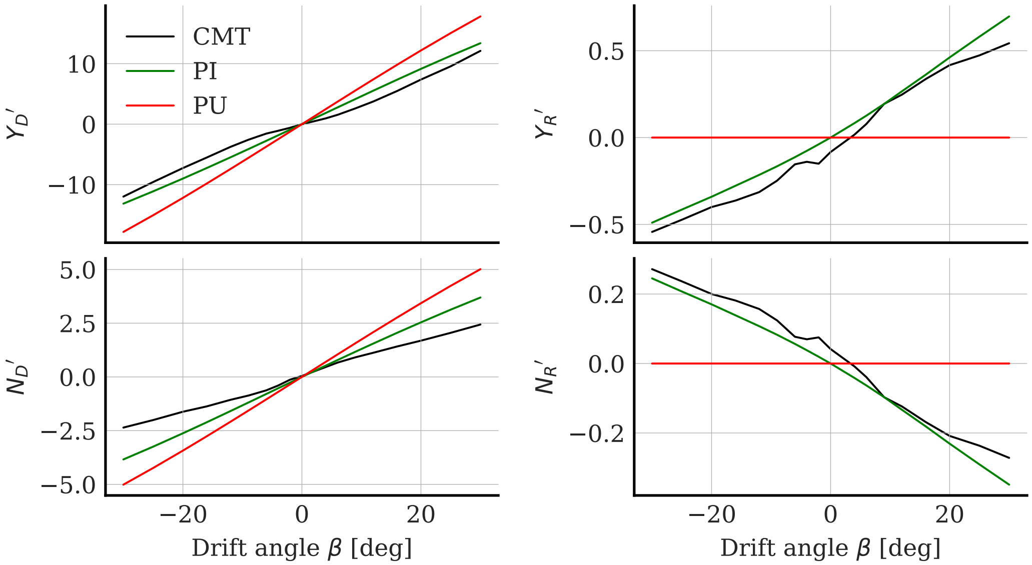

(a) Total forces.

(b) Rudder forces.

Fig. 17. KVLCC2 forces and moments (expressed in the prime system ×1000): HMRI CMTs (black), PI (green), and PU (red).

however larger disagreements for the KVLCC2 than the wPCC, which indicates that there may be some room for improvement of the proposed physics informed model, to better describe the hydrodynamics for other types of ships.

This paper did not treat the semi-empirical rudder as an entirely deterministic model. The flow straightening coefficients κ_v and κ_r were determined from the VCT and the rudder hull interaction coefficients a_H and x_H. For the time being, a few VCT calculations are thus needed. In the future, when more experience is gained about these coefficients, semi-empirical expressions or rules of thumb can hopefully be developed. The calculated rudder drag from the semi-empirical formulas and VCT were also not in good agreement. This did not greatly influence the overall results, but manual tuning was applied anyway. Further improvements on the semi-empirical formulations are thus needed to make the model fully deterministic.

CRediT authorship contribution statement

Martin Alexandersson: Writing – review & editing, Writing – original draft, Visualization, Validation, Software, Resources, Methodology, Investigation, Data curation. **Wengang Mao:** Writing – review & editing, Supervision, Project administration. **Jonas W. Ringsberg:** Writing – review & editing, Supervision. **Martin Kjellberg:** Writing – review & editing.

Declaration of competing interest

The authors declare that they have no known competing financial interests or personal relationships that could have appeared to influence the work reported in this paper.

Acknowledgements

The authors would like to acknowledge the financial support from Trafikverket/Lighthouse (grant id: FP4 2020) to prepare this paper. They would also thank all personnel at SSPA who have been involved in creating the model test results, building the ship models, and conducting the experiments.

Appendix A. Hull model

The hull forces are expressed with the following general polynomials, which are expressed in prime system units (see Section 2.3). The parameters omitted in this paper are also indicated.

$$X'_H = X'_0 + X'_{rr} r'^2 + X'_u u' + X'_{vr} r' v' + X'_{vv} v'^2 \tag{A.1}$$

$$Y'_H = Y'_0 + Y'_r r' + Y'_v v' + \cancel{Y'_{rrr}} r'^3 + \cancel{Y'_{vrr}} r'^2 v' + \cancel{Y'_{vvr}} r' v'^2 + \cancel{Y'_{vvv}} v'^3 \tag{A.2}$$

$$N'_H = N'_0 + N'_r r' + N'_v v' + \cancel{N'_{rrr}} r'^3 + \cancel{N'_{vrr}} r'^2 v' + \cancel{N'_{vvr}} r' v'^2 + \cancel{N'_{vvv}} v'^3 \tag{A.3}$$

Appendix B. Rudder models

B.1. Mathematical rudder model

The mathematical rudder model, used by the PU model, is expressed as a truncated third-order Taylor expansion, similar to Abkowitz (1964), as shown in Eq. (B.1)–Eq. (B.3).

$$X'_R = X'_{\delta\delta} \delta'^2 \tag{B.1}$$

$$Y'_R = Y'_{\delta\delta\delta} \delta'^3 + Y'_{\delta} \delta' + Y'_{r\delta\delta} \delta'^2 r' + Y'_{rr\delta} \delta' r'^2 + Y'_{v\delta\delta} \delta'^2 v' + Y'_{vr\delta} \delta' r' v' + Y'_{vv\delta} \delta' v'^2 \tag{B.2}$$

$$\begin{aligned} N'_R =& N'_{\delta\delta\delta} \delta'^3 + N'_{\delta} \delta' + N'_{r\delta\delta} \delta'^2 r' + N'_{rr\delta} \delta' r'^2 + N'_{v\delta\delta} \delta'^2 v' + N'_{vr\delta} \delta' r' v' \\ &+ N'_{vv\delta} \delta' v'^2 \end{aligned} \tag{B.3}$$

B.2. Semi-empirical rudder model

B.2.1. C_D

The drag coefficients for covered C_{DC} and uncovered C_{DU} are calculated with the similar equations: Eqs. (B.4) and (B.5), where C_{D0C} (Eq. (B.6)) and C_{D0U} (Eq. (B.7)) are the drag at zero rudder angle and

$e_0 = 0.9$ is the Oswald efficiency factor.

$$C_{DC} = C_{D0C} + \frac{C_{Dtune} C_L^2}{\pi A R_e e_0} \tag{B.4}$$

$$C_{DU} = C_{D0U} + \frac{C_{Dtune} C_L^2}{\pi A R_e e_0} \tag{B.5}$$

$$C_{D0C} = 2.5 C_{D0tune} C_{FC} \tag{B.6}$$

$$C_{D0U} = 2.5 C_{D0tune} C_{FU} \tag{B.7}$$

where C_{D0C} and C_{D0U} are different because of the different Reynolds number Re, as in Eq. (B.8)–Eq. (B.11).

$$C_{FC} = \frac{0.075 \log(10)^2}{\log\left(Re_{FC} - 2\right)^2} \tag{B.8}$$

$$C_{FU} = \frac{0.075 \log(10)^2}{\log\left(Re_{FU} - 2\right)^2} \tag{B.9}$$

$$Re_{FC} = \frac{V_{RC} c}{\nu} \tag{B.10}$$

$$Re_{FU} = \frac{V_{RU} c}{\nu} \tag{B.11}$$

B.2.2. Velocity in the propeller slip stream

According to momentum theory, the mean axial flow velocity far downstream of the propeller V_∞ is given by Eq. (B.12) (Brix, 1993), in which the thrust coefficient C_{Th} is calculated with Eq. (B.13), where r_0 is the propeller radius and the apparent velocity V_A is given by Eq. (B.14).

$$V_\infty = V_A \sqrt{C_{Th} + 1} \tag{B.12}$$

$$C_{Th} = \frac{2T}{\pi V_A^2 r_0^2 \rho} \tag{B.13}$$

$$V_A = u\left(1 - w_f\right) \tag{B.14}$$

The radius of the propeller slipstream far behind the propeller is given by Eq. (B.15).

$$r_\infty = r_0 \sqrt{\frac{V_A}{2 V_\infty} + \frac{1}{2}} \tag{B.15}$$

The velocity and the radius of the propeller slipstream at the position of the rudder can be calculated with Eq. (B.16) and Eq. (B.17), respectively, where x is the distance between the propeller and the rudder.

$$V_{xC} = \frac{V_\infty r_\infty^2}{r_x^2} \tag{B.16}$$

$$r_x = \frac{r_0 \left(\frac{r_\infty \left(\frac{x}{r_0}\right)^{1.5}}{r_0} + \frac{0.14 r_\infty^3}{r_0^3} \right)}{\left(\frac{x}{r_0}\right)^{1.5} + \frac{0.14 r_\infty^3}{r_0^3}} \tag{B.17}$$

Turbulent mixing of the slipstream and the surrounding flow will increase the radius r_x by r_Δ(Eq. (B.18)) so that a corrected axial velocity V_{xcorr} can be calculated according to Eq. (B.19).

$$r_\Delta = \frac{0.15 x \left(-V_A + V_{xC}\right)}{V_A + V_{xC}} \tag{B.18}$$

$$V_{xcorr} = V_A + \frac{r_x^2 \left(-V_A + V_{xC}\right)}{\left(r_\Delta + r_x\right)^2} \tag{B.19}$$

For a twin screw ship a small contribution from the yaw rate is also added to the velocity as seen in Eq. (B.20).

$$V_{RxC} = V_{xcorr} - r y_R \tag{B.20}$$

The velocity for the covered part of the rudder is obtained by Eq. (B.21).

$$V_{RC} = \sqrt{V_{RxC}^2 + V_{Ry}^2} \tag{B.21}$$

In addition, V_{xcorr} is used to calculate the lift diminished factor λ_R together with the expressions in Eq. (B.22)–Eq. (B.25).

$$\lambda_R = \left(\frac{V_A}{V_{xcorr}}\right)^f \tag{B.22}$$

$$f = \frac{512}{\left(2 + \frac{d}{c}\right)^8} \tag{B.23}$$

$$d = \frac{\sqrt{\pi}\left(r_\Delta + r_x\right)}{2} \tag{B.24}$$

$$c = \frac{c_r}{2} + \frac{c_t}{2} \tag{B.25}$$

B.2.3. Velocity outside the propeller slip stream

The axial velocity outside the propeller slip stream V_{xU} equals the apparent velocity (Eq. (B.26)). A small contribution from the yaw rate is also added for twin screw ships (Eq. (B.27)) so that the velocity outside the slip stream can be calculated with Eq. (B.28).

$$V_{xU} = V_A \tag{B.26}$$

$$V_{RxU} = V_{xU} - r y_R \tag{B.27}$$

$$V_{RU} = \sqrt{V_{RxU}^2 + V_{Ry}^2} \tag{B.28}$$

References

Abkowitz, M.A., 1964. Ship hydrodynamics - steering and manoeuvrability. Hydro- and Aerodynamics Laboratory, Hydrodynamics Section, Lyngby, Denmark, Report No. Hy-5, Lectures, URL: https://repository.tudelft.nl/islandora/object/uuid%3Ad511bd6b-ca2e-4f10-ad9f-6c881eb1e9f8.

Ahmed, F., Xiang, X., Jiang, C., Xiang, G., Yang, S., 2023. Survey on traditional and AI based estimation techniques for hydrodynamic coefficients of autonomous underwater vehicle. Ocean Eng. 268, 113300. http://dx.doi.org/10.1016/j.oceaneng.2022.113300, URL: https://www.sciencedirect.com/science/article/pii/S0029801822025835.

Alexandersson, M., 2024. wPCC Manoeuvring Model Tests, vol. 4, http://dx.doi.org/10.17632/j5zdrhr9bf.4, URL: https://data.mendeley.com/datasets/j5zdrhr9bf/4, Publisher: Mendeley Data.

Alexandersson, M., 2024a. Code for paper system identification of a physics-informed ship model for better predictions in wind conditions. 4, http://dx.doi.org/10.5281/zenodo.11577428.

Alexandersson, M., Mao, W., Ringsberg, J.W., 2022. System identification of vessel manoeuvring models. Ocean Eng. 266, http://dx.doi.org/10.1016/j.oceaneng.2022.112940, URL: https://www.sciencedirect.com/science/article/pii/S0029801822022235.

Aslam, S., Michaelides, M.P., Herodotou, H., 2020. Internet of ships: A survey on architectures, emerging applications, and challenges. IEEE Internet Things J. 7 (10), 9714–9727. http://dx.doi.org/10.1109/JIOT.2020.2993411, URL: https://ieeexplore.ieee.org/document/9090272/.

Brix, J.E., 1993. Manoeuvring Technical Manual. Seehafen-Verlag, ISBN: 978-3-87743-902-9, Google-Books-ID, CMJ1NAAACAAJ.

Faber, H., Soest, A.J.v., Kistemaker, D.A., 2018. Inverse dynamics of mechanical multibody systems: An improved algorithm that ensures consistency between kinematics and external forces. PLoS One 13 (9), e0204575. http://dx.doi.org/10.1371/journal.pone.0204575, URL: https://journals.plos.org/plosone/article?id=10.1371/journal.pone.0204575, Publisher: Public Library of Science.

Fossen, T.I., 2021. Handbook of Marine Craft Hydrodynamics and Motion Control, second ed. Wiley, Hoboken, NJ.

Haninger, K., Tomizuka, M., 2019-01-12. Nonparametric inverse dynamic models for multimodal interactive robots. http://dx.doi.org/10.48550/arXiv.1901.03872, arXiv:1901.03872, URL: http://arxiv.org/abs/1901.03872.

Hughes, M.J., Campbell, B.L., Belknap, W.F., Smith, T.C., 2011. TEMPEST Level-0 Theory:. Technical Report, Defense Technical Information Center, Fort Belvoir, VA, http://dx.doi.org/10.21236/ADA553545, URL: http://www.dtic.mil/docs/citations/ADA553545.

ITTC, 2017. Final Report and Recommendations to the 28th ITTC.

Jian-Chuan, Y., Zao-Jian, Z., Feng, X., 2015. Parametric identification of abkowitz model for ship maneuvering motion by using partial least squares regression. J. Offshore Mech. Arct. Eng. 137 (3), 031301. http://dx.doi.org/10.1115/1.4029827, URL: https://asmedigitalcollection.asme.org/offshoremechanics/article/doi/10.1115/1.4029827/377004/Parametric-Identification-of-Abkowitz-Model-for.

Kjellberg, M., Gerhardt, F., Werner, S., 2023. Sailing performance of wind-powered cargo vessel in unsteady conditions. J. Sail. Technol. 8 (01), 218–254. http://dx.doi.org/10.5957/jst/2023.8.12.218.

Kurtz, V., Castro, A., Önol, A.Ö., Lin, H., 2023-10-11. Inverse dynamics trajectory optimization for contact-implicit model predictive control. http://dx.doi.org/10.48550/arXiv.2309.01813, arXiv:2309.01813, URL: http://arxiv.org/abs/2309.01813.

Lewis, E.V., 1989. Principles of Naval Architecture Second Revision. The Society of Naval Architects and Marine Engineers.

Li, S., Liu, C., Chu, X., Zheng, M., Wang, Z., Kan, J., 2022. Ship maneuverability modeling and numerical prediction using CFD with body force propeller. Ocean Eng. 264, http://dx.doi.org/10.1016/j.oceaneng.2022.112454.

Liu, Y., Zou, L., Zou, Z., Guo, H., 2018. Predictions of ship maneuverability based on virtual captive model tests. Eng. Appl. Comput. Fluid Mech. 12, 334–353. http://dx.doi.org/10.1080/19942060.2018.1439773.

Lorenz, E.N., 1963. Deterministic nonperiodic flow. J. Atmos. Sci. 20 (2), 130–141. http://dx.doi.org/10.1175/1520-0469(1963)020<0130:DNF>2.0.CO;2, URL: https://journals.ametsoc.org/view/journals/atsc/20/2/1520-0469_1963_020_0130_dnf_2_0_co_2.xml, Publisher: American Meteorological Society Section: Journal of the Atmospheric Sciences.

Luo, W., 2016. Parameter identifiability of ship manoeuvring modeling using system identification. Math. Probl. Eng. 2016, e8909170. http://dx.doi.org/10.1155/2016/8909170, URL: https://www.hindawi.com/journals/mpe/2016/8909170/, Publisher: Hindawi.

Marimon Giovannetti, L., Olsson, F., Alexandersson, M., Werner, S., Finnsg˚ard, C., 2020. The Effects of Hydrodynamic Forces on Maneuvrability Coefficients for Wind-Assisted Ships. http://dx.doi.org/10.1115/OMAE2020-18673.

Mastalli, C., Chhatoi, S.P., Corbères, T., Tonneau, S., Vijayakumar, S., 2023-03-23. Inverse-dynamics MPC via nullspace resolution. http://dx.doi.org/10.48550/arXiv.2209.05375, arXiv:2209.05375, URL: http://arxiv.org/abs/2209.05375.

Matusiak, J., 2021. Dynamics of a Rigid Ship - With Applications, third ed. URL: https://aaltodoc.aalto.fi:443/handle/123456789/108000.

Miller, A., 2021. Ship model identification with genetic algorithm tuning. Appl. Sci. 11 (12), 5504. http://dx.doi.org/10.3390/app11125504, URL: https://www.mdpi.com/2076-3417/11/12/5504.

Nomoto, K., Taguchi, T., Honda, K., Hirano, S., 1957. On the steering qualities of ships. In: International Shipbuilding Progress, ISP, vol. 4, (no. 35), Osaka University, Department of Naval Architecture, Japan, pp. 354–370, 1957, URL: https://repository.tudelft.nl/islandora/object/uuid%3Ae8c24e2b-1a9c-48f2-b56d-1ad6b047a6c7.

Norrbin, N.H., 1971. Theory and observations on the use of a mathematical model for ship manoeuvring in deep and confined waters. In: Proceedings of the 8th Symposium on Naval Hydrodynamics, ONR, Pasadena, California. Publication 68 of the Swedish State Shipbuilding Experimental Tank, Göteborg, Sweden, pp. 807–905, URL: https://repository.tudelft.nl/islandora/object/uuid%3A75736a6f-66e1-4c00-b3bc-897a19a232ea.

Stern, F., Agdraup, K., Kim, S.Y., Hochbaum, A.C., Rhee, K.P., Quadvlieg, F., Perdon, P., Hino, T., Broglia, R., Gorski, J., 2011. Experience from SIMMAN 2008—The First Workshop on Verification and Validation of Ship Maneuvering Simulation Methods. J. Ship Res. 55 (02), 135–147. http://dx.doi.org/10.5957/jsr.2011.55.2.135, URL: https://onepetro.org/JSR/article/55/02/135/173675/Experience-from-SIMMAN-2008-The-First-Workshop-on.

Sun, G., Ding, Y., 2023-11-01. High-order inverse dynamics of serial robots based on projective geometric algebra. Multibody Syst. Dyn. 59 (3), 337–362. http://dx.doi.org/10.1007/s11044-023-09915-7.

Villa, D., Franceschi, A., Viviani, M., 2020. Numerical analysis of the rudder–propeller interaction. J. Mar. Sci. Eng. 8 (12), 990. http://dx.doi.org/10.3390/jmse8120990, URL: https://www.mdpi.com/2077-1312/8/12/990, Number: 12 Publisher: Multidisciplinary Digital Publishing Institute.

Whicker, L.F., Fehlner, L.F., 1958. Free-Stream Characteristics of A Family of Low-Aspect-Ratio, All-Movable Control Surfaces for Application to Ship Design:. Technical Report, Defense Technical Information Center, Fort Belvoir, VA, http://dx.doi.org/10.21236/ADA014272, URL: http://www.dtic.mil/docs/citations/ADA014272.

Yasukawa, H., Yoshimura, Y., 2015. Introduction of MMG standard method for ship maneuvering predictions. J. Mar. Sci. Technol. 20 (1), 37–52. http://dx.doi.org/10.1007/s00773-014-0293-y.